A Bifurcation Analysis of Neuronal Subthreshold Oscillations

John A. White,* Thomas Budde,‡ and Alan R. Kay‡
*Department of Biomedical Engineering, Boston University, Boston, Massachusetts; and ‡Department of Biological Sciences, University of Iowa, Iowa City, Iowa USA

ABSTRACT The conditions under which a noninactivating sodium current and either a potassium current or an inwardly rectifying cation current can generate subthreshold oscillations were analyzed using nonlinear dynamical techniques applied to a neuronal model consisting of two differential equations. Mathematical descriptions of the membrane currents were derived using voltage-clamp data collected from entorhinal cortical neurons. A bifurcation analysis was performed using applied current as the control parameter to map the range of magnitudes of the sodium, potassium/cation, and leakage conductances over which subthreshold oscillations exist. The threshold of the potassium/cation current was an important determinant of the robustness of oscillatory behavior. The activation time constant of the potassium/cation current largely determined the frequency range of emergent oscillations. This result implicates the slow inward rectifier or an as yet undescribed slow outward current in entorhinal cortical oscillations; the latter explanation, while more speculative, is more consistent with the pharmacological properties of subthreshold oscillations and gives oscillations over a larger current range. The shallowness of the sodium activation curve confined emergent oscillations to rise gradually rather than abruptly and extended the current range over which the model oscillated.

INTRODUCTION

Synchronized neural oscillations have been implicated in higher brain functions as diverse as feature binding, learning and memory, and even consciousness (Crick and Koch, 1990; Singer, 1993). Within the hippocampal region, synchronized activity in the range of 4–12 Hz, the so-called θ (theta)-rhythm, is associated with exploratory behavior (Vanderwolf, 1969). θ-like neural activity is important in inducing both long-term potentiation and long-term depression (Christie and Abraham, 1992; Larson and Lynch, 1986), and thus the θ rhythm may play a role in the mnemonic functions of the hippocampal formation.

Within the hippocampal region, stellate neurons in layer II of the medial entorhinal cortex (mEC) exhibit ~8-Hz oscillations in response to subthreshold constant-current stimuli in vitro (Alonso and Klink, 1993; Alonso and Llinás, 1989). With increasing depolarizing current, these oscillations arise gradually out of the noise in the membrane-potential range from −60 to −52 mV. (Resting potential is about −60 mV.) Oscillatory frequency is within the frequency range of the θ-rhythm and only mildly dependent on current level within the subthreshold range. Action potentials are phase-locked with the oscillations for suprathreshold stimuli (Alonso and Klink, 1993; Alonso and Llinás, 1989). Thus, it has been proposed that these subthreshold oscillations contribute to θ-rhythm activity in vivo (Alonso and Klink, 1993; Alonso and Llinás, 1989; Bland and Colom, 1993). Subthreshold oscillations are abolished by tetrodotoxin (TTX) and by blockers of the delayed K^+ conductance (Klink and Alonso, 1993), indicating that this slow neural rhythm is controlled by a (noninactivating) Na^+ current and the delayed rectifier.

In this study we have used theoretical techniques to explore what sort of hyperpolarizing current, which, when combined with the persistent sodium current, could generate slow oscillations of the appropriate form. Two forms of currents are likely candidates: the above-mentioned delayed rectifier, the threshold of which is sensitive to modulatory state (Eder et al., 1991); and the slow inward-rectifying cation current that is present in these neurons (Alonso and Klink, 1993; Klink and Alonso, 1993). Our strategy was to use several forms of the hyperpolarizing current (e.g., low- and high-threshold delayed K^+ currents, the slow inward rectifier), while generally holding constant the activation properties of the known persistent sodium current. In one case (series D), potassium current kinetics were held constant and the form of the sodium current was changed. For each model type (or "series"), oscillatory behavior was examined over a large range of maximal sodium, potassium/cation, and leak conductances. In each series, general oscillatory properties over the parameter space were compared with electrophysiological data from layer II cells of the entorhinal cortex, particularly with regard to oscillatory period. Although our analysis focused on these particular neurons, it also serves as a more general analysis of mechanisms underlying oscillations in a two-conductance model.

Following the experiments of Alonso and colleagues (Alonso and Klink, 1993; Alonso and Llinás, 1989), models were analyzed by finding bifurcation points (points at which system behavior changes qualitatively) as applied current (the bifurcation parameter) was increased. In particular, we sought parameters for which

Received for publication 6 December 1994 and in final form 3 July 1995.
Address reprint requests to John A. White, Department of Biomedical Engineering, Boston University, 44 Cummington Street, Boston, MA 02215. Tel.: 617-353-5903; Fax: 617-353-6766; E-mail: jwhite@ bu.edu.

0006-3495/95/10/1203/15 $2.00

the amplitude of the oscillation increased gradually from zero (or near zero) and oscillatory frequency was stable with increasing applied current, mirroring the form of subthreshold oscillations in layer II cells. This restriction confined our analyses to supercritical Hopf bifurcations and a subpopulation of subcritical Hopf bifurcations (Strogatz, 1994). In our analyses we paid attention to the robustness of hypothetical mechanisms in the face of small perturbations in parameters. Oscillatory behavior that is not robust in this sense would not be reliable under physiological conditions.

This study has four parts. First, we established experimentally the presence of a persistent Na^+ current in the mEC and developed a quantitative description of this current. Second, given the context of known properties of delayed K^+ currents in these neurons, we examined the specific effects of the threshold and activation time constant of the K^+ current on subthreshold oscillatory behavior. Third, we assessed the effects of the unusually shallow Na^+ current activation on modeled oscillations. Finally, we tested the alternative hypothesis that the slow inward rectifying cation current (the h current I_h), rather than the delayed K^+ current, underlies subthreshold oscillations. Part 1 was accomplished using the whole-cell patch-clamp technique to record from acutely isolated neurons. Parts 2–4 were accomplished by applying dynamical systems theory to a mathematical model of subthreshold oscillations.

MATERIALS AND METHODS

Experimental methods

Experiments were performed in acutely dissociated neurons from the superficial mEC of mature rats, using methods described previously (White et al., 1993). Briefly, Long-Evans rats (male, 4–7 weeks old), were decapitated (both with and without anesthesia) and the brain rapidly removed and placed in a beaker of ice-cold, oxygenated dissociation medium containing (in mM): NaCl 115, KCl 5, $CaCl_2$ 1, $MgCl_2$ 4, PIPES 20, glucose 25, pH = 7.0 (with NaOH). The brain was blocked and horizontal brain slices were made through the dorso-ventral extent of the entorhinal cortex using a Vibratome (Ted Pella, Inc., Redding, CA). Each brain slice was trimmed down to a piece containing only the superficial layers of the mEC. Neurons were isolated mechanically from these trimmed slices after enzymatic treatment with proteinase K (0.2 mg/ml for 5 min; P-0390, Sigma Chemical Co., St. Louis, MO) and trypsin (1 mg/ml for 30 min; T-1005, Sigma Chemical Co.).

Acutely dissociated neurons were transferred to a 300 μl recording chamber. After the neurons had settled to the bottom of the chamber, the dissociation solution was replaced with an initial recording solution. The control recording solution contained (in mM): NaCl 120, CsCl 5, $CaCl_2$ 2, $MgCl_2$ 2, tetraethylammonium chloride 15, 4-aminopyridine 5, HEPES 10, and D-glucose 25, pH = 7.4. To this solution low concentrations of TTX were added to block and hence pharmacologically isolate the persistent Na^+ current.

Electrical recordings were obtained using the whole-cell patch technique and an Axopatch amplifier (200 or 200A; Axon Instruments, Foster City, CA). Recording pipettes had series resistances of 1–2.5 MΩ. Most recordings were performed using an electrode solution containing (in mM): CsF 120, NaCl 15, HEPES 10, and EGTA 11, pH = 7.25. Results were verified using an electrode solution containing (in mM): $CsMeSO_4$ 110, NaCl 15, HEPES acid 10, EGTA 11, $CaCl_2$ 1, $MgCl_2$ 2, $ATPNa_2$ 2, pH = 7.25. After breaking through the cell membrane, the experimenter waited at least 5 min for the kinetics and magnitudes of membrane currents to stabilize before collecting data. Corrections for pipette and cell capacitance and series resistance, made at the beginning of the recording session, were monitored and, if necessary, adjusted, every few minutes during the course of the recording session. Voltages were not corrected for liquid junction potentials. Data were filtered using a low-pass Bessel filter with a slope of 80 dB/decade and a cutoff frequency of 5 kHz and digitized using Clampex (Axon Instruments). Corrections for leakage conductance were made during off-line data analysis. All recordings were performed at room temperature (22–24°C).

Development of the model

The neuronal model used to study subthreshold oscillatory behavior was of the same form as that used by Morris and Lecar (1981). The model has two voltage-dependent conductances: one selective for Na^+ and one selective for K^+. (In one model series (series E), the second conductance was a less specific, inwardly rectifying cation conductance.) The Na^+ conductance, which activates much faster than does the K^+ conductance, is assumed to activate instantaneously, reducing the number of ordinary differential equations to two:

$$\frac{dv}{dt} = -g_{Na}m_\infty(v)(v - 1) - g_K w(v - v_K) - g_L(v - v_L) + i_{app} \quad (1)$$

$$\frac{dw}{dt} = \phi\frac{w_\infty(v) - w}{\tau_w(v)} \quad (2)$$

This reduction in the number of dependent variables does not alter significantly the behavior of the system (Krinskii and Kokoz, 1973; Morris and Lecar, 1981; Plant and Kim, 1976; see the Discussion and Fig. 12). The voltage-dependent functions $m_\infty(v)$, $w_\infty(v)$, and $\tau_w(v)$ are given by:

$$m_\infty(v) = 0.5 \cdot [1 + \tanh\{(v - v_1)/v_2\}] \quad (3)$$

$$w_\infty(v) = 0.5 \cdot [1 + \tanh\{(v - v_3)/v_4\}] \quad (4)$$

$$\tau_w(v) = 1/\cosh\{(v - v_3)/(2 \cdot v_4)\} \quad (5)$$

Eqs. 1–5 are in the dimensionless form used by Rinzel and Ermentrout (1989; see Appendix). Eq. 1 represents current flow through each membrane conductance and the voltage-clamp electrode. Eq. 2 describes w, the activation function of the K^+ current. The terms in Eqs. 1–5 are defined in Table 1.

Parameters describing the Na^+ current were derived from our data (see Fig. 1, Table 2). Parameters describing the K^+ current were derived from previously published data (Eder et al., 1991). Parameters describing I_h, the inward rectifier, were derived from recordings in cultured neocortical neurons (Budde et al., 1994). In all cases, Boltzman function representations of activation functions were converted to hyperbolic tangent form. The Boltzman function representation can be rewritten:

$$\frac{1}{1 + e^{-x}} = \frac{e^{x/2}}{e^{x/2} + e^{-x/2}} = 0.5\left[1 + \frac{e^{x/2} - e^{-x/2}}{e^{x/2} + e^{-x/2}}\right]$$

$$= 0.5[1 + \tanh(x/2)]$$

Modeling methods

In each model series (A–E; see Results and Table 2), the conductances g_{Na}, g_K, and g_L were varied over a rectangular grid (for g_{Na}: 0.04, 0.08, . . . , 2.0; for g_K: 0.4, 0.8, . . . , 20.0; for g_L: 0.1, 0.2, . . . , 2.0). For each point in g_{Na}-g_K-g_L space, v_L was adjusted to make Eq. 1 = 0 when $v = -1.25$ and $i_{app} = 0$. This manipulation served two purposes. First, it gave each

TABLE 1 Definitions of terms

Term	Definition
v	Normalized membrane potential
w	Activation variable of the K^+/cation conductance
g_{Na}	Maximal sodium conductance
g_K	Maximal K^+/cation conductance
g_L	Leak conductance
v_K	Reversal potential of the K^+/cation conductance
v_L	Reversal potential of the leak conductance
ϕ	Time-scaling parameter (=0.2)
$m_\infty(v)$	Steady-state activation function of the sodium conductance
$w_\infty(v)$	Steady-state activation function of the K^+/cation conductance
$\tau_w(v)$	Activation time constant of the K^+/cation conductance
v_1	Half-activation voltage of the Na^+ conductance
v_2	Slope of the Na^+ activation function
v_3	Half-activation voltage of the K^+/cation conductance
v_4	Slope of the K^+/cation activation function
i_{app}	Applied current
i_{bif1}, i_{bif2}	Leftmost and rightmost bifurcation currents
$\lambda_{1,2}$	The two eigenvalues associated with a critical point
P	Dimensionless oscillatory period
P^*	Normalized oscillatory period = ϕP = (dimensional period)/τ_{max}
τ_{max}	Maximal value of the dimensional activation time constant of w, in seconds

All terms except τ_{max} are dimensionless. See Appendix for the normalization procedure.

model a "resting potential" of −1.25, corresponding to the in vitro resting potential of −60 mV (although this "resting potential" was not always stable). Second, setting the resting critical point to −1.25 made all models oscillate in the same general range of g_{Na}-g_K-g_L-space, making it easier to compare behavior after various manipulations. Models in which the calculated value of v_L was less than −2.0 were rejected; this condition, corresponding in the dimensional system to $V_L < -96$ mV, is not physiologically realistic.

Bifurcation analysis was performed using modified code from the program AUTO (Doedel, 1981). Using applied current as the bifurcation parameter, the bifurcation behavior was determined for each case. When a bifurcation was encountered, it was flagged as either a Hopf or saddle-node bifurcation (Strogatz, 1994). (Pitchfork bifurcations were not seen.) For Hopf bifurcations, an additional run was made from the bifurcation point to determine the stability, magnitude, and period of ensuing oscillations. Floquet multipliers were calculated so that supercritical and subcritical Hopf bifurcations (which give rise to gradually and abruptly arising oscillations, respectively; see Results) could be distinguished. For subcritical Hopf bifurcations, the half-magnitude of the abruptly appearing oscillation was calculated and saved.

Phase-plane analyses and time-domain simulations were performed using the program XPP (Rinzel and Ermentrout, 1989). For time-domain simulations, the Adams predictor-corrector integration method was used. All modeling and simulations were performed on a UNIX workstation (Hewlett-Packard 720, Sun Sparcstation 2, or Silicon Graphics Indy).

RESULTS

The persistent Na^+ current in neurons from the superficial medial entorhinal cortex

Crucial to our efforts to test the hypothesis that the persistent Na^+ current and delayed K^+ current underlie subthreshold oscillations in mEC stellate neurons are quantitative descriptions of those currents. The delayed K^+ current has been described before (Eder et al., 1991), but it was necessary for us to collect the data describing the persistent Na^+ current (I_p). We used slow voltage-ramp stimuli (100 mV/10 s) to isolate the persistent Na^+ current from its inactivating counterpart and as a convenient way to generate the current-voltage relationship for the persistent current from two stimulus presentations (one in control conditions, one in the presence of the blocking agent TTX). Fig. 1 *A* shows the current-voltage relationship of I_p in one neuron, derived by subtracting slow voltage-ramp responses collected in 300 nM TTX from control responses. The solid squares at 5-mV intervals represent recorded data; the solid line is a least-squares fit of a Boltzman function multiplied by a driving force term ($G_{Na}/(1 + e^{(V - V0)/dV})$ $(V - V_{Na})$; for this example, $V_0 = -45.7$ mV, $dV = -6.87$ mV, $V_{Na} = 38.1$ mV). This I-V relationship is notable for its low threshold. Fig. 1 *B* shows an I_p activation curve, generated using averaged values of V_0 (mean = −53.8 mV; SEM = 2.7 mV; $n = 3$) and dV (mean = −5.15 mV; SEM = 1.3 mV; $n = 3$). This model activation curve was converted to hyperbolic tangent form (see rewritten Boltzman function representation, above) and used in model series A–D. Solid squares and error bars represent mean values ± standard errors of activation (g/g_{max}) for the three instances of I_p. For comparative purposes, the figure shows activation curves derived for the TTX-resistant, inactivating Na^+ current in mEC neurons (White et al., 1993) and the persistent Na^+ current in Purkinje cells of the cerebellum (A. R. Kay, M. Sugimori, and R. R. Llinás, manuscript in preparation). I_p of the mEC differs from the other currents in two regards. Its half-activation voltage is much lower than that of the TTX-resistant Na^+ current. The two persistent Na^+ currents have similar half-activation voltages, but the mEC current has a shallower activation function, and hence a lower threshold, than its counterpart in the cerebellum.

Preliminary analysis of bifurcation behavior

Because the system described by Eqs. 1–5 has only two state variables (w and v), its behavior can be examined conveniently in the phase plane. Fig. 2 *A* shows the nullclines (curves for which *dv/dt* and *dw/dt* = 0, respectively) in w-v space for different values of i_{app}. Increasing i_{app} shifts the *dv/dt* nullcline upward (Fig. 2, *solid lines*) but has no effect on the *dw/dt* nullcline (Fig. 2, *dashed line*). The boxed region in Fig. 2 *A* is expanded in Fig. 2 *B* to show more clearly the critical points where the *dw/dt* and *dv/dt* nullclines intersect.

The stability of a critical point (v,w) can be assessed by linearizing about that point and determining the resulting eigenvalues. For this system of equations, the eigenvalues are given by the following equation (Rinzel and Ermentrout, 1989):

$$\lambda_{1,2} = 0.5 \cdot [a + d + \sqrt{(a + d)^2 - 4(ad - bc)}] \quad (6)$$

where

$$a = -g_{Na}\left[\frac{\bar{v}-1}{2v_2\cosh\frac{\bar{v}-v_1}{v_2}} + 0.5\left(1+\tanh\frac{\bar{v}-v_1}{v_2}\right)\right] - g_K\bar{w} - g_L \quad (7)$$

$$b = -g_K(\bar{v}-v_K) \quad (8)$$

$$c = \frac{0.5\cdot\phi}{v_4}\cdot\cosh\frac{\bar{v}-v_3}{2v_4}\operatorname{sech}^2\frac{\bar{v}-v_3}{v_4} \quad (9)$$

$$d = -\phi\cosh\frac{\bar{v}-v_K}{2v_4} \quad (10)$$

With $i_{app} = 0$, $\lambda_{1,2} = -0.21 \pm 0.44i$. Since the real part of λ_1 and λ_2 (Re(λ)) is less than 0, this critical point is stable; the corresponding time-domain trace (Fig. 2 *B*, *bottom right*) begins at $v = -1.20$ and oscillates only transiently before settling at resting potential (−1.25). With $i_{app} = 0.03$, Re(λ) = −0.08, implying that this critical point is also stable; the corresponding time-domain trace (Fig. 2 *B*, *middle right*) approaches the new critical point via a damped oscillation. With $i_{app} = 0.06$, Re(λ) = 0.04 > 0, implying that this critical point is unstable. The time-domain response (Fig. 2 *B*, *top right*) will oscillate indefinitely.

Fig. 2 *C* shows a bifurcation diagram for the model. In this plot, v is plotted versus the bifurcation parameter i_{app}. The solid line at the lower left indicates a region in which the critical point is stable. At $i_{app} = i_{bif1} \approx 0.05$, the critical point becomes unstable (Fig. 2 *C*, *dashed line*) and a stable limit cycle arises via a supercritical Hopf bifurcation. The maximum and minimum values of the limit-cycle oscillation, as a function of applied current, are represented by the curved dashed-and-dotted lines (labeled "osc") extending from i_{bif1} to i_{bif2}. For a supercritical Hopf bifurcation, oscillations begin with zero amplitude, just as in recordings from EC stellate cells (Alonso and Klink, 1993; Alonso and Llinás, 1989). At $i_{app} = i_{bif2} \approx 0.13$, the limit cycle collapses onto another trajectory of stable critical points via another supercritical Hopf bifurcation.

Fig. 2 *D* is a bifurcation diagram for a model with a different set of conductances ($g_{Na} = 0.68$, $g_K = 2.0$, $g_L = 1.8$). This model exhibits two subcritical Hopf bifurcations. When i_{app} exceeds i_{bif1}, arising oscillations are at first unstable (Fig. 2 *D*, *dotted line*). The system will converge to the envelope represented by the dashed-and-dotted lines (labeled "osc"). Thus, for a subcritical bifurcation, oscillations will emerge with nonzero ampli-

TABLE 2 Model parameters

Series	v_1	v_2	v_3	v_4	v_K
A	−1.12	0.21	−0.14	0.50	−1.63
B	−1.12	0.21	−0.50	0.81	−1.63
C	−1.12	0.21	−1.0	0.81	−1.63
D	−1.12	0.10	−1.0	0.81	−1.63
E	−1.12	0.21	−1.83	−0.39	−0.67

Parameters are defined in Table 1.

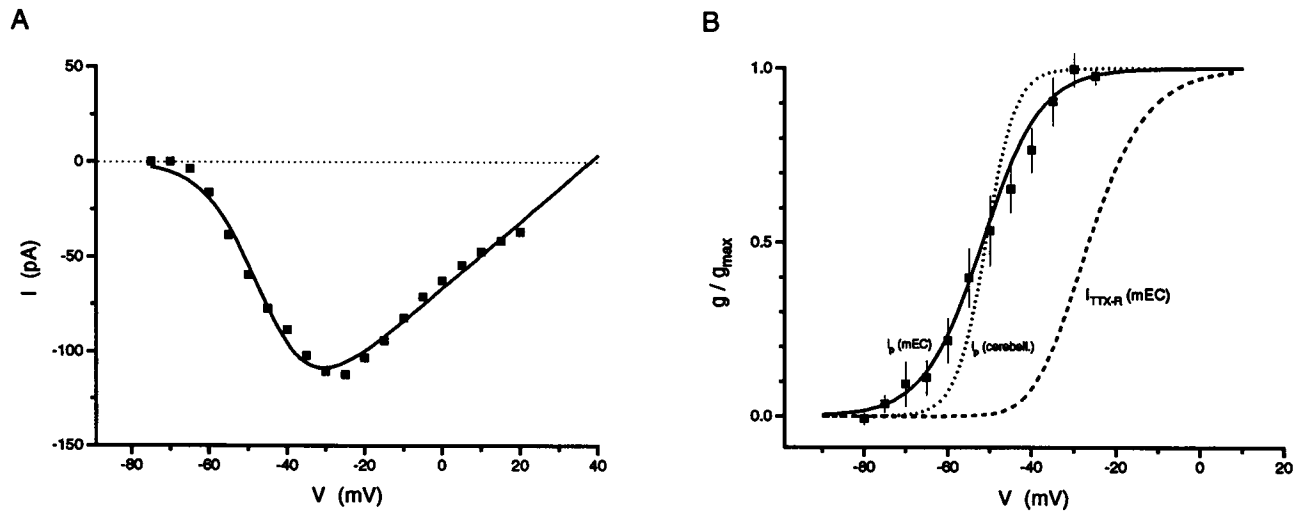

FIGURE 1 The persistent Na^+ current in the medial entorhinal cortex. (*A*) Current-voltage relationship for the persistent Na^+ current (I_p) from one neuron in the superficial mEC, generated using a slow voltage ramp (100 mV/10 s). Discrete points were obtained by subtracting data collected in 300 nM TTX from control data. The smooth curve is a least-squares fit of a Boltzman function multiplied by a factor representing driving force. See the text for more details. (*B*) Steady-state values of conductance for three Na^+ conductances, plotted versus voltage-clamp potential. Squares and error bars are mean ±SEM for I_P in three mEC neurons. (——) An activation curve derived from average half-activation potentials and slopes for I_p in the mEC. (· · · · ·) A similarly derived curve for I_p in cerebellar Purkinje cells (A. R. Kay, M. Sugimori, and R. R. Llinás, manuscript in preparation). The dashed line is the activation curve for $I_{TTX\text{-}R}$, the inactivating, TTX-resistant Na^+ conductance from the mEC (White et al., 1993). This relationship was estimated from the peak value of this conductance.

tude. This behavior contrasts with oscillations seen in EC stellate cells (Alonso and Klink, 1993; Alonso and Llinás, 1989), although it is important to note that subcritically generated oscillations with small initial amplitude could be indistinguishable from supercritically generated oscillations in practice.

At a Hopf bifurcation point, the period of emergent oscillations is inversely related to the magnitude of the imaginary component of the eigenvalue λ (Rinzel and Ermentrout, 1989; Strogatz, 1994). In this case:

$$P = \frac{2\pi}{\sqrt{\phi\cosh\frac{\bar{v}-v_3}{2v_4}\left[g_{Na}\left((\bar{v}-1)\left(\frac{1}{2v_2}\right)\operatorname{sech}^2\frac{\bar{v}-v_1}{v_2}+0.5\left(1+\tanh\frac{\bar{v}-v_1}{v_2}\right)\right)+g_K\bar{w}+g_L+g_K(\bar{v}-v_K)\left(\frac{1}{2v_4}\right)\operatorname{sech}^2\frac{\bar{v}-v_3}{v_4}\right]}} \quad (11)$$

(This equation applies to observed oscillations only for supercritical Hopf bifurcations.) Eq. 11 can be re-expressed by examining Eqs. 6–11 more closely. At a Hopf bifurcation point, λ is purely imaginary, because $a + d$ (from Eq. 6) is 0 and the term inside the radical is negative. Thus, at a Hopf bifurcation point, we have the relationship:

$$g_{Na}\left((\bar{v}-1)\left(\frac{1}{2v_2}\right)\operatorname{sech}^2\frac{\bar{v}-v_1}{v_2}+0.5\left(1+\tanh\frac{\bar{v}-v_1}{v_2}\right)\right) + g_K\bar{w}+g_L = -\phi\cosh\frac{\bar{v}-v_3}{2v_4} \quad (12)$$

Using this equation, we can derive:

$$P = \frac{2\pi\tau_w(\bar{v})}{\phi}\left\{\frac{g_K(\bar{v}-v_K)}{2v_4\phi}\left[\frac{\tau_w(\bar{v})^5}{(2-\tau_w(\bar{v})^2)^2}\right]^{-1}\right\}^{-1/2} \quad (13)$$

From Eq. 13, we would expect P to be on the same scale as $2\pi\tau_w/\phi$ as long as the term in the radical is near one. To make $P \gg 2\pi\tau_w/\phi$, we need to drive the term in the radical to near 0. We might expect that this is possible under some circumstances, but if the term in the radical of Eq. 13 is driven to near 0, a small perturbation in any parameter could make the term negative (and, equivalently, drive the term inside the radical of Eq. 11 negative). This condition implies that the term in the radical of Eq. 6 is positive. As a result, both eigenvalues would be real and the oscillations would disappear. Thus, we would expect that large-period oscillations are possible under certain conditions, but that these slow oscillations would be prone to disappearing with small perturbations in parameters.

Large-period oscillations in a two-dimensional system can also be generated via a saddle-node bifurcation (Rinzel and Ermentrout, 1989; Strogatz, 1994). Fig. 3 *A* shows the nullclines for a model that generates a saddle-node bifurcation (with $g_{Na} = 0.44$, $g_K = 0.8$, $g_L = 1.4$). The boxed region of Fig. 3 *A* is shown at higher magnification in Fig. 3 *B*. For $i_{app} = 0$ (Fig. 3 *B*, *lower solid nullcline*), the system has only one critical point at resting potential. At $i_{app} = 0.065$, (Fig. 3 *B*, *middle solid nullcline*), there are three critical points. Two are stable (Fig. 3 *B*, *solid circles*) and one is a saddle point (Fig. 3 *B*, *open triangle*). Saddle points, characterized by one (real) positive eigenvalue and one (real) negative eigenvalue, are unstable. As i_{app} is increased further, the saddle point and lower stable point merge and disappear at the saddle-node bifurcation. The top solid nullcline in Fig. 3, *A* and *B* illustrates a state just past the bifurcation point.

Fig. 3 *C* shows the bifurcation diagram for this model. The saddle-node bifurcation is the point at which the bifurcation curve traces backward and becomes unstable. This model has a region of bistability and exhibits a subcritical Hopf bifurcation, but the emergent unstable oscillations (maximum and minimum values shown (Fig. 3 *C*, *dotted lines*) intersect the trajectory of unstable critical points (Fig. 3 *C*, *dashed line*) and hence disappear before they stabilize. Thus, this model does not exhibit observable oscillatory behavior. Even when stable oscillations do appear via saddle-node bifurcations, they emerge with large amplitude and have periods that are highly dependent on applied current (Rinzel and Ermentrout, 1989; Strogatz, 1994), and thus are not physiologically relevant for our application. We marked saddle-node bifurcations in our analysis but did not analyze them further.

Mapping bifurcation behavior in g_{Na}-g_K space

Bifurcation behavior with the control model (series A)

The bifurcation behavior of the neural model with control K^+-conductance data from Eder et al. (1991) was examined in series A (see Table 2). Fig. 4 *A1* shows maps of bifurcation behavior for this model, corresponding to the lowest (0.1), middle (1.0), and highest (2.0) values of the leakage conductance examined. Six types of behavior are mapped. First, for many points, shown in dark gray on the bifurcation maps, $v_L < -2.0$, corresponding to a dimensional reversal potential < -96 mV. We did not analyze these cases further because they lack physiological relevance. Second, for large values of g_{Na} relative to g_K, the resting critical point at $v = -1.25$ itself was unstable, leading to spontaneous oscillations at "rest." These "spontaneously active" points are labeled in medium gray. Third, for small values of g_{Na} relative to g_K, oscillations would not arise regardless of the amount of de-

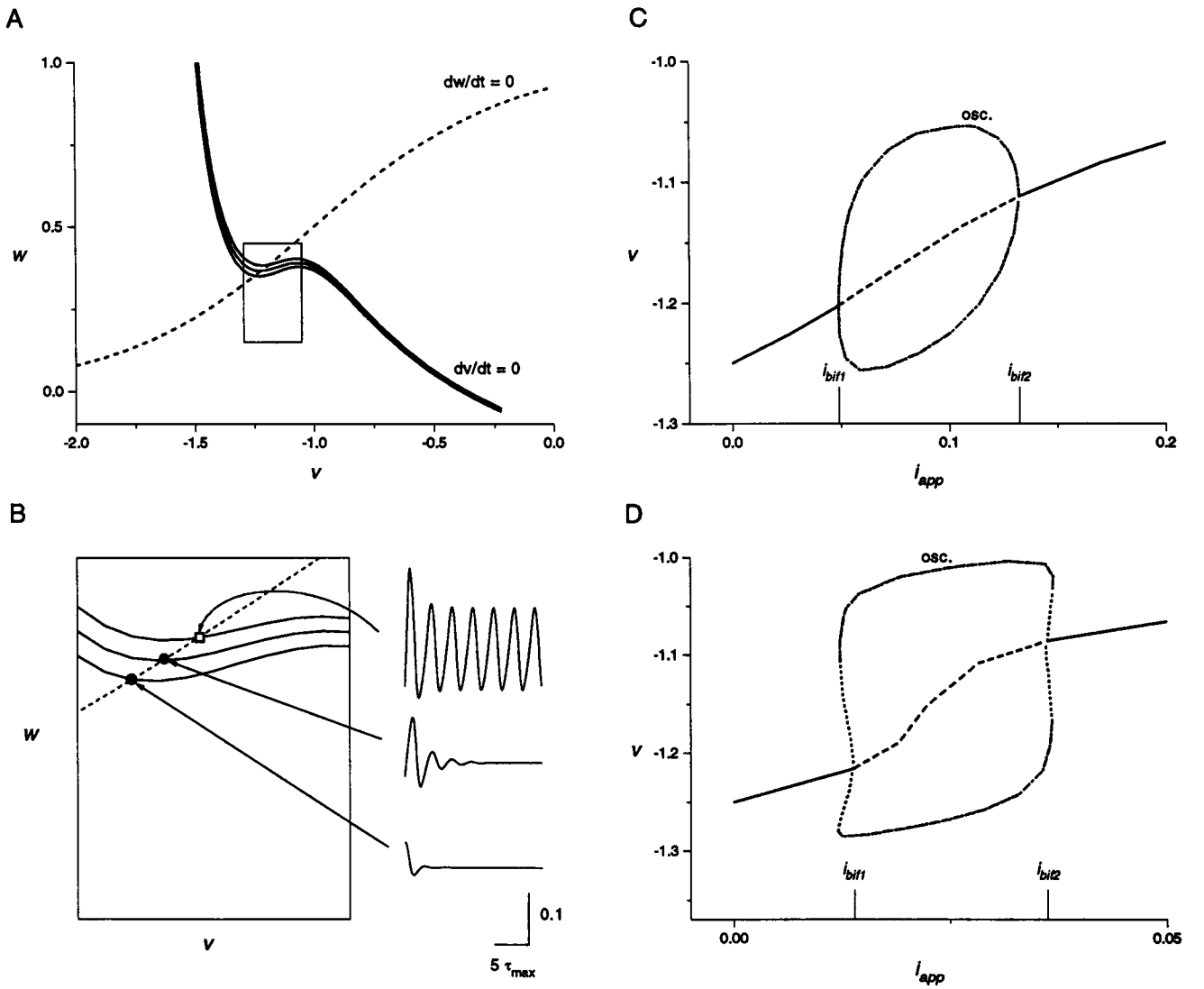

FIGURE 2 Oscillatory behavior for specific instances of the Morris-Lecar model. (*A*) Phase plane for the Morris-Lecar model (Eqs. 1–5) with $v_1 = -1.12$, $v_2 = 0.21$, $v_3 = -1.0$, $v_4 = 0.81$, $g_{Na} = 0.8$, $g_K = 4.4$, $g_L = 1.5$, $\phi = 0.2$, $v_K = -1.63$, $v_L = -1.129$. The curves are nullclines corresponding to the two dependent variables (—— for v and - - - - for w). From bottom to top, the three $dv/dt = 0$ nullclines correspond to $i_{app} = 0.0$, 0.03, and 0.06, respectively. (*B*) A magnified view of the box in A. Each critical point is marked as stable (●) or unstable (□). To the far right are corresponding time-domain responses (v vs. t), with time scaled by τ_{max}, the maximal value of the dimensional activation time constant for w. From bottom to top these responses correspond to applied current values of 0.0 (with $v_0 = -1.20$), 0.03 (with $v_0 = -1.25$), and 0.06 (with $v_0 = -1.25$). (*C*) A bifurcation diagram for this model. For $i_{app} < 0.049$ and >0.132, the model has a stable critical point (——). At $i_{app} = i_{bif1} \approx 0.049$, this critical point becomes unstable (- - - - -), and oscillations emerge via a supercritical Hopf bifurcation. The maximum and minimum values of the oscillations are plotted as the dashed-and-dotted line marked "osc." At $i_{app} = i_{bif2} \approx 0.132$, the oscillations disappear via another supercritical Hopf bifurcation. (*D*) A bifurcation diagram for a model with $g_{Na} = 0.68$, $g_K = 2.0$, $g_L = 1.8$, $v_L = -1.293$. At $i_{app} = i_{bif1}$, unstable oscillations (· · · ·) emerge via a subcritical Hopf bifurcation. The trajectory of unstable oscillations leads to one of stable oscillations (· · · · · · ·). The bifurcation at i_{bif2} is subcritical as well.

polarizing current injected. These points, labeled "No Bif." (Fig. 4), are color-coded light gray. For intermediate values of g_{Na} relative to g_K, the model could generate oscillations via Hopf bifurcations, either subcritical (abruptly appearing; Fig. 4, *yellow points*) or supercritical (gradually rising; Fig. 4, *blue points*). The model in series A is notable for generating oscillations very rarely. Finally, some models (Fig. 4, *red points*) exhibited saddle-node bifurcations, a condition that can lead to oscillations, but not of the correct form for our application. These cases were not analyzed further.

Effects of shifting the K^+ activation curve (series B and C)

Eder et al. (1991) saw changes in the threshold of the delayed K+ current with time and attributed these changes to neuromodulation. In series B, we generated additional maps of bifurcation behavior using "modulated" rather than "control" delayed K^+ current. Relative to the control K^+ current, the modulated current is left-shifted (by ~17 mV in dimensional terms) and has a shallower slope. In contrast with the series A model, the series B model can generate oscillations over a still

modest but appreciable range of values of g_{Na} and g_K (Fig. 4 *B1*). In fact, counted over the entire range of simulations, the changes in K^+ current activation increased the number of parameter sets exhibiting supercritical Hopf bifurcations more than sevenfold (from 167 to 1223; Fig. 5). This trend continues if the threshold of the delayed K^+ current is shifted further. In series C, v_3 was changed from -0.50 to -1.0, effectively shifting the K^+ activation curve 24 mV in the hyperpolarizing direction. This modification makes oscillatory behavior yet more robust (2416 parameter sets exhibiting supercritical Hopf bifurcations; Fig. 5).

Periods of emergent oscillations

At a Hopf bifurcation point, the period of the emergent oscillation can be calculated using Eq. 11. Fig. 6, *A1–C1*, shows histograms of the periods associated with all Hopf bifurcations for series A–C, respectively. Each period value has been normalized by dividing by the maximal value of the K^+ activation time constant. (This value = $1/\phi$ for the dimensionless model, or τ_{max} for the dimensional model; see Appendix.) Printed in each panel are the number of Hopf bifurcations (n) found in 50,000 parameter sets; the number of such bifurcations with normalized period (P^*) < 5; and the number with $P^* > 10$.

The few oscillations that do occur in series A are mostly of relatively low period; only 42 of 248 have $P^* > 10$. Series B and C show more robust oscillatory behavior, but nearly all of these oscillations are confined to relatively low periods. In series B (Fig. 6 *C1*), 94% (1209 of 1282) of oscillations have $P^* < 5$, and only 13 of 1282 have $P^* > 10$. In series C (Fig. 6 *C1*), 98% of oscillations have $P^* < 5$, and only 3 of 2703 have $P^* > 10$. Since the delayed K^+ current has $\tau_{max} < 7$ ms, as indicated by voltage-clamp (Eder et al., 1991; J. A. White and A. R. Kay, unpublished data) and current-clamp (Klink and Alonso, 1993) data, the results in Fig. 6 indicate that oscillations generated by this outward current should largely be confined to periods below $5 \times \tau_{max} = 35$ ms, implying oscillatory frequencies >28 Hz.

As described above, the oscillations represented in the top row of Fig. 6 include large, suddenly arising oscillations generated by subcritical Hopf bifurcations and not relevant to the behavior described in current-clamp recordings (Alonso and Llinás, 1989; Alonso and Klink, 1993). Fig. 6, *A2–C2*, shows period histograms for only the supercritical bifurcations and those subcritical bifurcations that become stable with half-amplitude less than 0.125 (corresponding to ~6 mV). Periods of supercritical oscillations were calculated as before. For small subcritical oscillations, we desired not the period at the bifurcation point but the period of the first stable oscillation. These periods were calculated numerically using AUTO (Doedel, 1981). Confining our analysis to small oscillations made little difference in the distributions of periods.

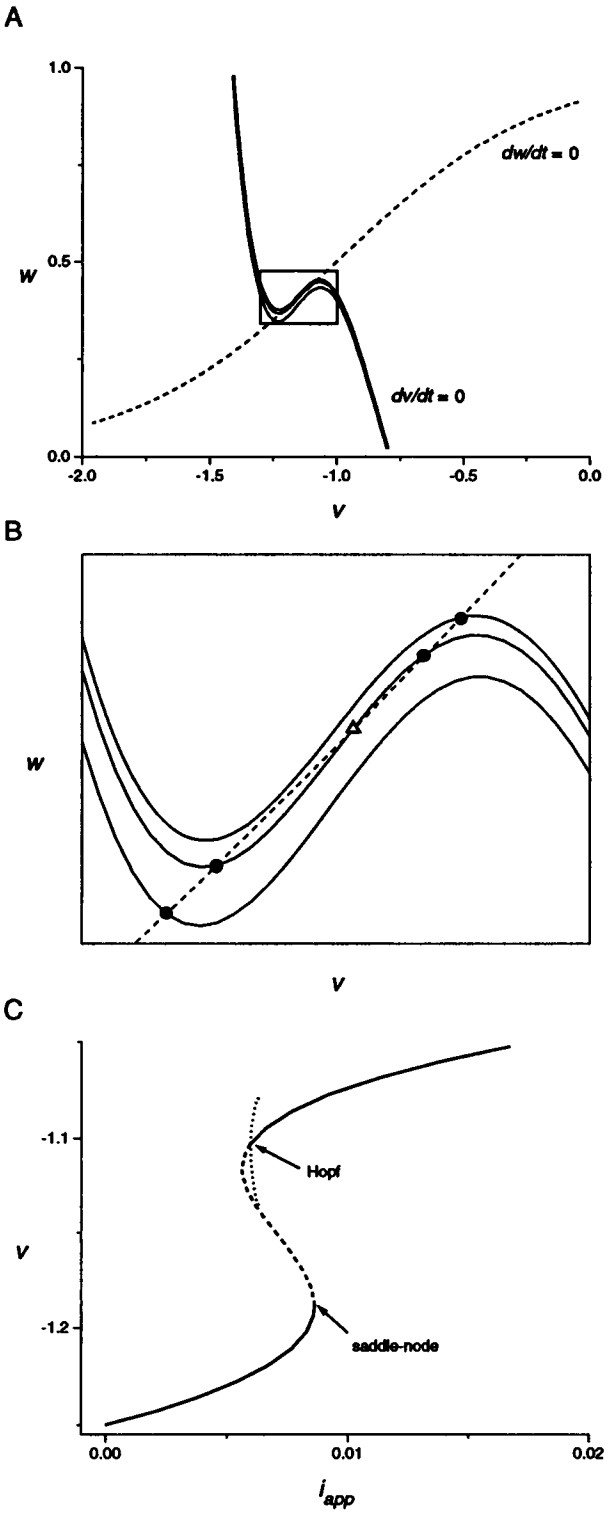

FIGURE 3 Saddle-node bifurcations in the model. (*A*) Phase plane for the model with $v_1 = -1.12$, $v_2 = 0.21$, $v_3 = -1.0$, $v_4 = 0.81$, $g_{Na} = 0.44$, $g_K = 0.8$, $g_L = 1.4$, $\phi = 0.2$, $v_K = -1.63$, $v_L = -1.129$. (- - - -) *dw/dt* nullcline. (——) *dv/dt* nullclines. From bottom to top, the three *dv/dt* = 0 nullclines correspond to $i_{app} = 0.0$, 0.0065, and 0.0095, respectively. (*B*) Magnified view of the inset in *A*. (●) Stable critical points. (△) Saddle point. See text. (*C*) Bifurcation diagram for the model, exhibiting a saddle-node bifurcation and a subcritical Hopf bifurcation. (——) Stable points. (- - - -) Unstable points. (· · · ·) Maximum and minimum values of unstable oscillations.

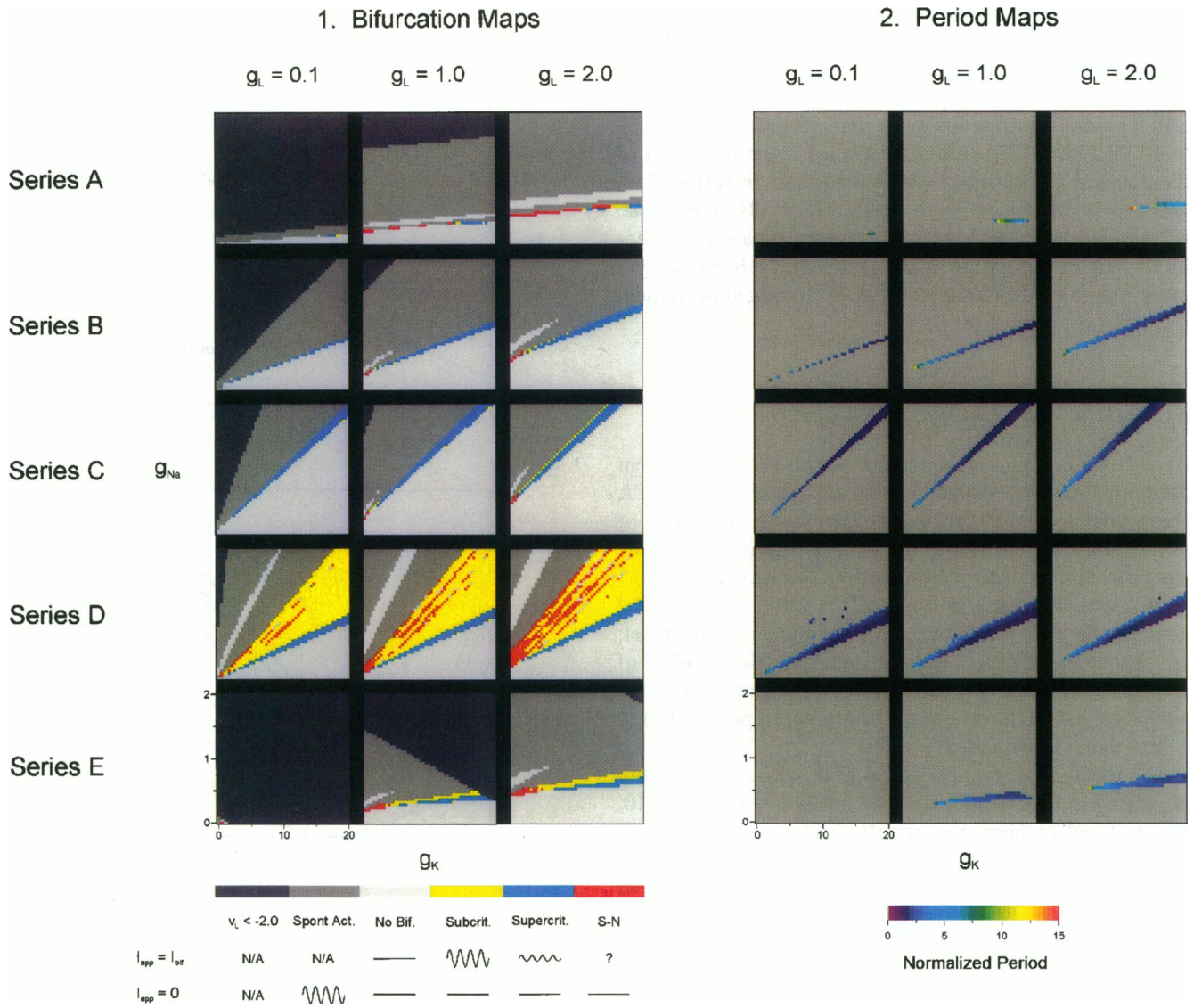

FIGURE 4 Maps of bifurcation behavior and oscillatory period. (*Left side, A1–E1*): Bifurcation maps for model series A–E (see text and Table 2). Each row shows plots for three values of g_L (0.1, 1.0, and 2.0). In each map, the x axis represents the range g_K = 0–20; the y axis represents the range g_{Na} = 0–2. The color code is given at the bottom. ($v_L < -2.0$, *dark gray*) Models for which the calculated value of v_L is <-2.0. (Spont. Act., *medium gray*) Models that spontaneously oscillate at "rest". (No Bif., *light gray*) Models that do not oscillate at any value of i_{app}. (Subcrit., *yellow*) Models exhibiting subcritical Hopf bifurcations. (Supercrit., *blue*) Models exhibiting supercritical Hopf bifurcations. (S-N, *red*) Models exhibiting saddle-node bifurcations. (*Right side, A2–E2*) Period maps for small oscillations (all oscillations generated via supercritical Hopf bifurcations and those oscillations generated via subcritical Hopf bifurcations that stabilize with half-magnitude < 0.125). x and y axes are the same as in *A1–E1*. Normalized period is plotted on a pseudocolor scale (see scale bar). Gray regions represent models that do not exhibit small oscillations.

The histograms in Fig. 6, *A2–C2*, are again dominated by low-period oscillations, implying that oscillations generated by the delayed K^+ current largely have fundamental frequencies >28 Hz.

To gain insight into the relationship between conductance values and the periods of emergent small oscillations, we plotted maps of normalized period P^* on a pseudocolor scale on the right side of Fig. 4. The gray areas of each map represent regions in which the model did not generate small oscillations from a stable resting potential (cf. Fig. 4, *left side*). Rows A–E of the graph again represent series A–E, respectively, of Table 2. (Series D and E are discussed below.) In all cases, the highest-period oscillations are confined to the lower left of the oscillatory regime. As the wedge-shaped surface extends to higher conductance values, it broadens and period values drop. The period maps of Fig. 4 re-emphasize the fact that oscillatory periods are almost exclusively confined to the scale of τ_w (in other words, they do not greatly exceed τ_{max}, which is <7 ms for the delayed K^+ current). This result is an important one, for it implies that relatively fast K^+ conductances can underlie slow (i.e., large-period) oscillations only in rare cases (see above). The robustness of the many small-period and few

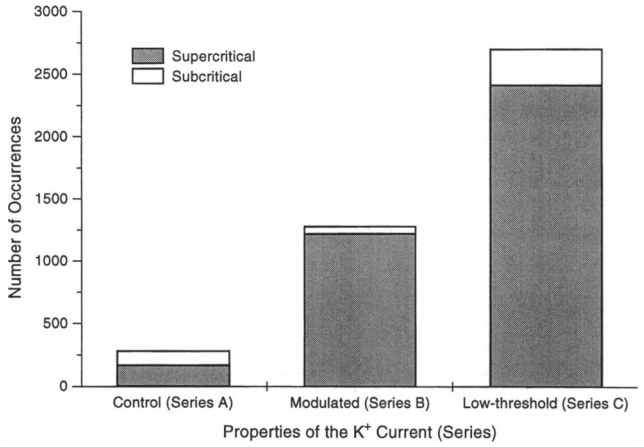

FIGURE 5 Effects of properties of the K^+ current on bifurcation behavior. Plotted are the number of supercritical (*shaded*) and subcritical (*white*) Hopf bifurcations exhibited over the entire g_{Na}-g_K-g_L space for series A–C.

large-period oscillations generated by the model are examined below.

Stability of oscillations with fluctuations in parameters

Comparative stability of series A, B, and C

It is unlikely that intracellular mechanisms that regulate channel density clearly are accurate to three decimal places. Therefore, in addition to the number of oscillations of a given kind and frequency range exhibited by a given series of models, it is important to know the stability of these oscillations in the face of perturbations of model parameters. To this end, we systematically perturbed one model parameter (g_{Na}; only one parameter was perturbed systematically because of the large computational load of this analysis) at each bifurcation point from the analysis summarized in the right side of Fig. 4 and determined whether or not the small oscillations survived the perturbations. Fig. 7 *A* summarizes the results of these perturbations. For series A, ±5% perturbations in g_{Na} both led to 76% decreases in the number of small oscillations. Series B and C were progressively more resistant to this manipulation. For example, a +5% perturbation in g_{Na} led a 64% decrease in the number of small oscillations for series B and a 46% decrease for series C (Fig. 7 *A*).

For those oscillations that survived in Fig. 7 *A*, the stability of oscillatory period was also examined. As shown in Fig. 7 *B*, the period of small oscillations for series A was systematically sensitive to small perturbations in g_{Na}. Interestingly, the slope of P versus g_{Na} is the opposite of what one would expect; normally, an increase in g_{Na} would make the system more "excitable" and decrease P. In contrast to results from series A, the oscillatory period in series B and C was largely insensitive to changes in g_{Na} for those oscillations that survived the manipulation. (Results from series C overlie those from series B and are not plotted.) Thus, it can be concluded that oscillations generated by the high-threshold K^+ current of series A are not robust in three regards. First, small oscillations occurred in only 235 of 50,000 cases examined in series A. Second, oscillations generated in series A were prone to disappearing with small perturbations in g_{Na}. Third, the period of surviving oscillations from series A were particularly sensitive to changes in g_{Na}. Oscillations generated in series B and C were progressively more robust in all three regards, as suggested by the thickness of the swaths of small oscillations in Fig. 4, *A2–C2*.

Comparative stability of low- and high-period oscillations

From Fig. 7 *B*, one would expect that mean oscillatory periods would increase linearly with perturbations in g_{Na}. In fact, this is not the case. In series C, e.g., the mean oscillatory period is 1.97 under control conditions, but decreases to 1.93 with a +5% perturbation in g_{Na} and to 1.84 with a −5% perturbation in g_{Na}. This nonmonotonic relationship is due to the fact that, although oscillatory periods do on the whole increase with increasing g_{Na}, large-period oscillations are preferentially obliterated by small perturbations in g_{Na}. In series C, e.g., 82% of small oscillations with $P^* < 5$ (35 ms in dimensional terms) survive both +1% and −1% perturbations in g_{Na}. In contrast, none of the small oscillations with $P^* > 10$ survive this insult, apparently because of reasons suggested above in our discussion of Eqs. 6–13.

The effects of g_{Na} and g_K on stability and P^* are demonstrated for three specific models in Fig. 8, *A* and *B*. For the two large-period models (model A1 from series A and model C1 from series C; see Fig. 8 legend for parameters), progressive reductions in g_{Na} (Fig. 8 *A*) lead to decreases in period, and even 1% increases in g_{Na} obliterate the oscillatory behavior, as indicated by the disappearance of the trace for $g_{Na} > 100\%$ of control. The effect of perturbations in g_K (Fig. 8 *B*) is the opposite. Decreasing g_K obliterates the large-period oscillations; increasing g_K decreases the period of oscillation. An important consequence of these relationships is that large-period oscillations occur only in a small window around specific values of both g_{Na} and g_K (and g_L as well; data not shown).

Small-period oscillations, representing the great majority of the total (Figs. 4 and 6), are much more robust than their large-period counterparts. For example, model C2 of Fig. 8, *A* and *B* oscillates at the same period with ±5% perturbations in either g_{Na} or g_K. Thus, stable oscillatory behavior is obtained within a relatively broad window of conductance values.

Eqs. 11 and 13 describe the period at the bifurcation point, but another important issue is whether or not oscillatory period changes radically as i_{app} increases beyond i_{bif1}. Fig. 8 *C* shows the bifurcation diagram for model C1 (Fig. 8 *C*, *left axis*). Normalized period P^* (Fig. 8 *C*, *dotted line, right axis*) is plotted as well. At $i_{app} = i_{bif1}$, $P^* = 21.6$, but P^* decreases monotonically as i_{app} is increased. This behavior is summarized for three models in Fig. 8 *D*, in which

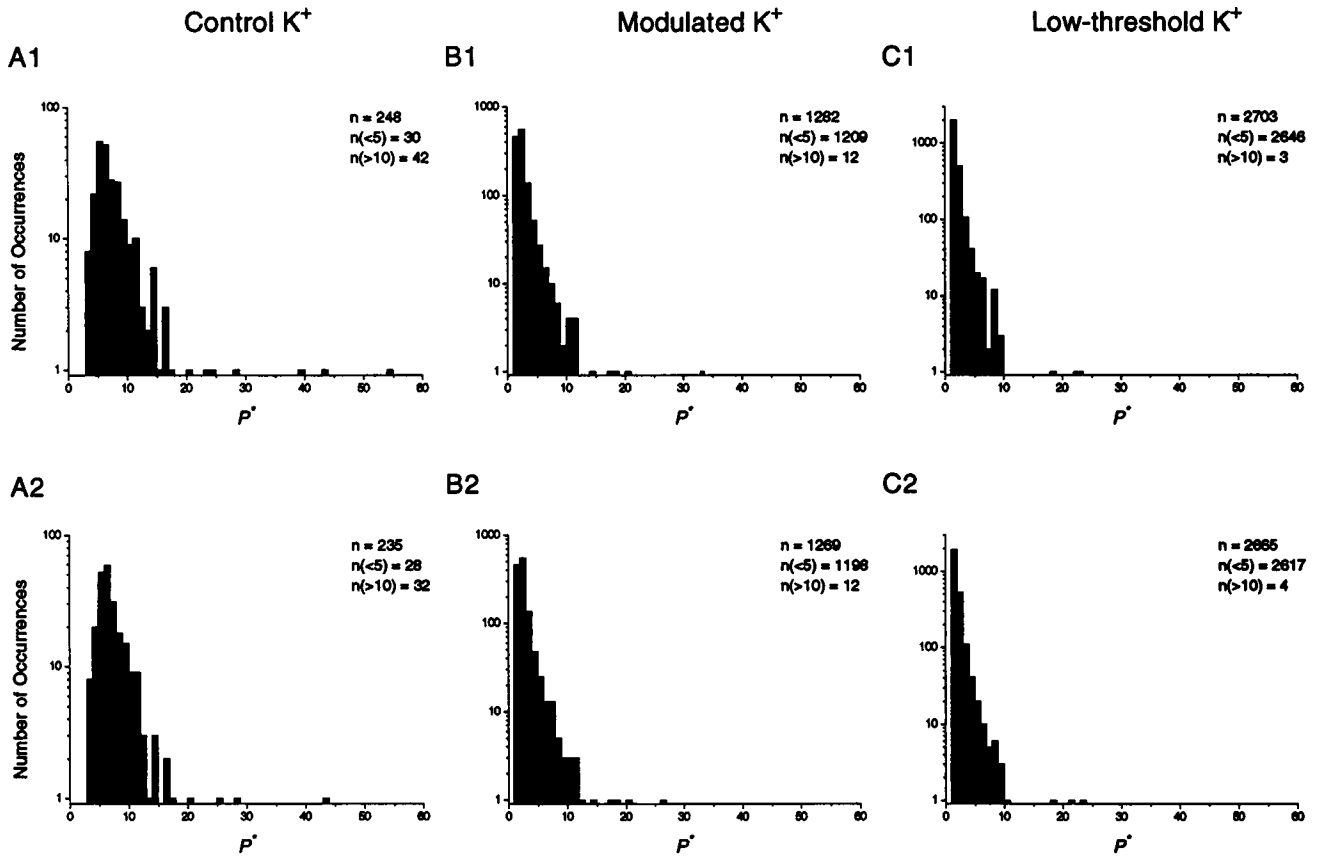

FIGURE 6 Effects of K^+ current properties on oscillatory period. (*Top row, A1–C1*) Histograms of normalized oscillatory period (P^*) at Hopf bifurcation points for series A (*A1*), B (*B1*), and C (*C1*). Printed in the inset of each panel is the number of Hopf bifurcations (n), the number of these bifurcations with $P^* < 5$, and the number with $P^* > 10$. (*Bottom row, A2–C2*) Histograms of P^* for small oscillations exhibited by series A–C. See text.

P^* is plotted versus v_{peak}, the difference between the peak voltage and voltage at i_{bif1}. For the high-period models (Fig. 8 *D*, *A1* and *C1*), P^* decreases rapidly as the oscillations increase in magnitude. In contrast, P^* versus v_{peak} is stable for low-period oscillations generated by model C2, mimicking physiological results (Alonso and Klink, 1993).

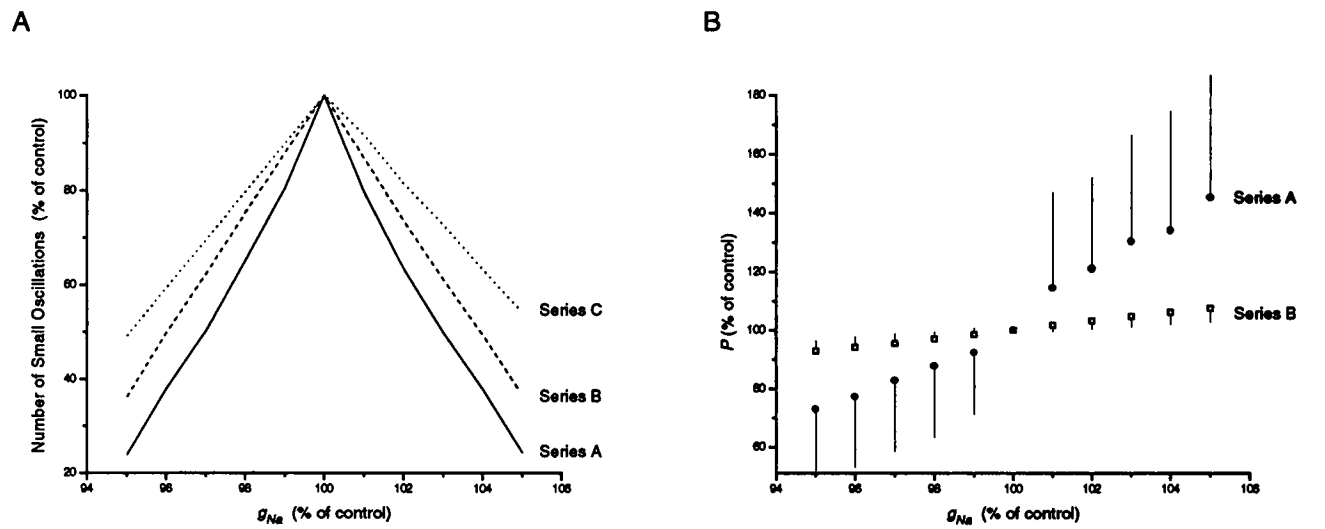

FIGURE 7 Effects of perturbations in g_{Na} on oscillatory behavior in series A–C. (*A*) Number of small oscillations exhibited by series A–C in response to perturbation of g_{Na} from its control value, expressed as a percent of control. Control values: 235 (series A); 1269 (series B); 2665 (series C). (*B*) Effect of perturbations in g_{Na} on the periods of small oscillations for series A and B. Error bars represent standard deviations. Results for series C are indistinguishable from results for series B, with the exception that standard deviations are smaller for series C.

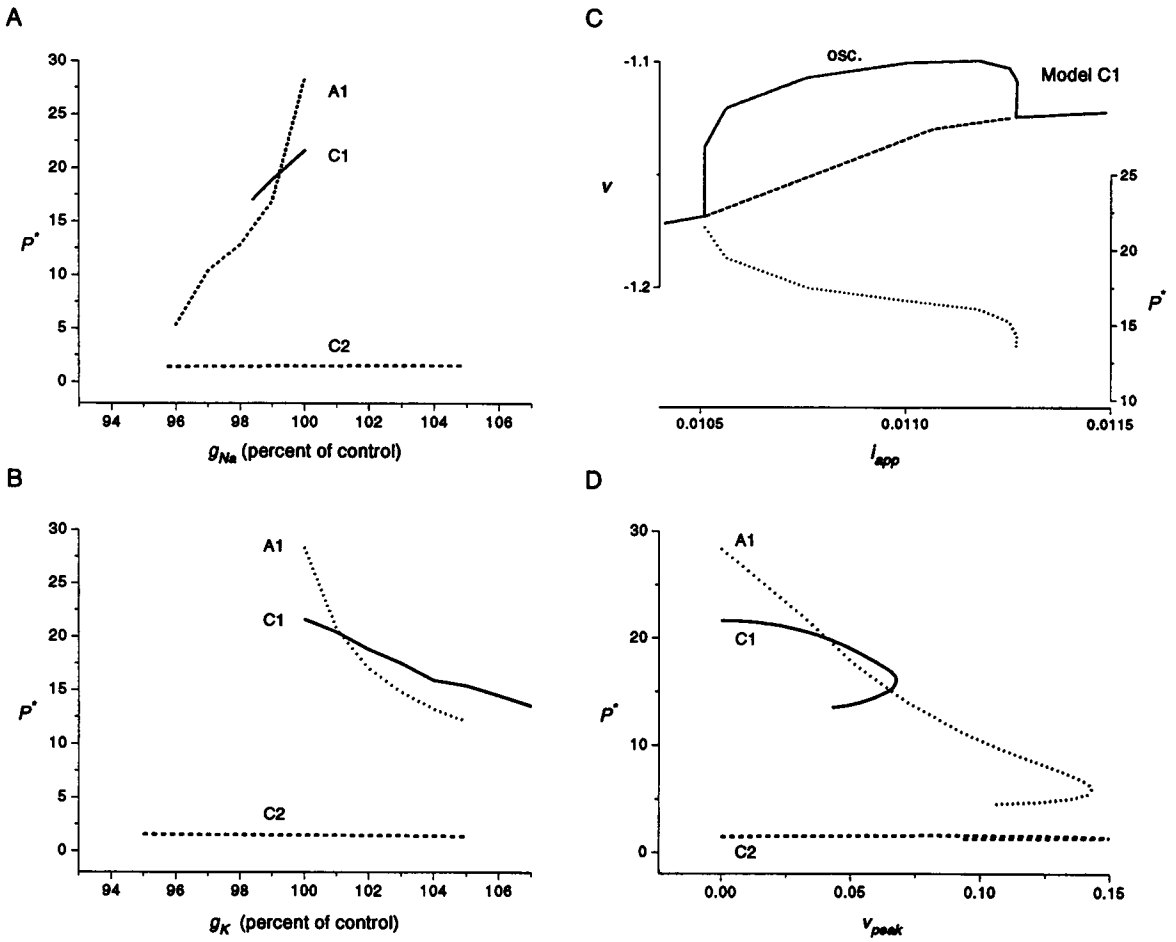

FIGURE 8 Large-period oscillations are unstable. (*A* and *B*) Plots of P^* in response to perturbations in either g_{Na} (*A*) or g_K (*B*) for three models (A1, C1, and C2; see below). Model A1 oscillates in the 96–100% range for g_{Na} and the 100–105% range for g_K. Model C1 oscillates in the 98.4–100% range for g_{Na} and the 100–107% range for g_K. Model C2 oscillates in the 95.7–105% range for g_{Na} and the 95–105% range for g_K. (*C*) Bifurcation diagram for model C1. (——) Stable critical points. (- - - -) Unstable critical points. The symbols indicate the maximum deflection of a stable limit cycle. Numbers indicate the normalized period at a given point. (*D*) Plots of P^* versus v_{peak}, defined as the maximum deflection of the limit cycle from the bifurcation membrane potential, for three models. Model A1: from series A, with (g_{Na}, g_K, g_L) = (0.24, 13.6, 0.5). Model C1: from series C, with (g_{Na}, g_K, g_L) = (0.36, 0.8, 1.10). Model C2: from series C, with (g_{Na}, g_K, g_L) = (1.64, 16.0, 0.5).

Effects of steepness of the Na^+ conductance activation curve (series D)

The persistent Na^+ current in the mEC has a significantly shallower activation function than its counterpart in cerebellar Purkinje cells (Fig. 1 *B*). To examine the effects of such differences in slope, we performed a series of simulations with the activation curve of the Na^+ current made twice as steep (series D in Table 2). As shown in Fig. 4 *D1*, the principal effect of this manipulation on bifurcation behavior is to add a large region of subcritical bifurcations to the bifurcation map. Thus, series D is particularly prone to large, abruptly appearing oscillations. Nevertheless, series D shows a large region of small oscillations (Figs. 4 *D2*, 9 *A*), with P^* confined mostly to the range of 1–5 times the maximum value of τ_w (Fig. 9 *A*). Series D exhibited no small oscillations with $P^* > 9$.

The effects of perturbations in g_{Na} on series D oscillations were examined and are summarized in Fig. 10. Series D oscillations were more robust in the face of this perturbation than oscillations generated by series A–C; only 24% of small oscillations were obliterated with g_{Na} at 105% of control (Fig. 10 *A*). However, the oscillatory period was more sensitive to g_{Na} in series D than in series B or C (Fig. 10 *B*; cf. Fig. 7 *B*).

Behavior of an alternative model with a hyperpolarization-activated current (I_h) (series E)

Periods of robust oscillations exhibited by the Morris-Lecar model are normally in the range of 1–5 times τ_{max}, the maximal value of the K^+ conductance activation time constant. Since $\tau_{max} < 7$ ms for this membrane conductance, its kinetics are too fast to underlie 8-Hz subthreshold oscillations under the conditions modeled. Several alternative explanations can be advanced to explain intrinsic low-frequency oscillations (see Discussion). One of these is that the slow, hyperpolarization-

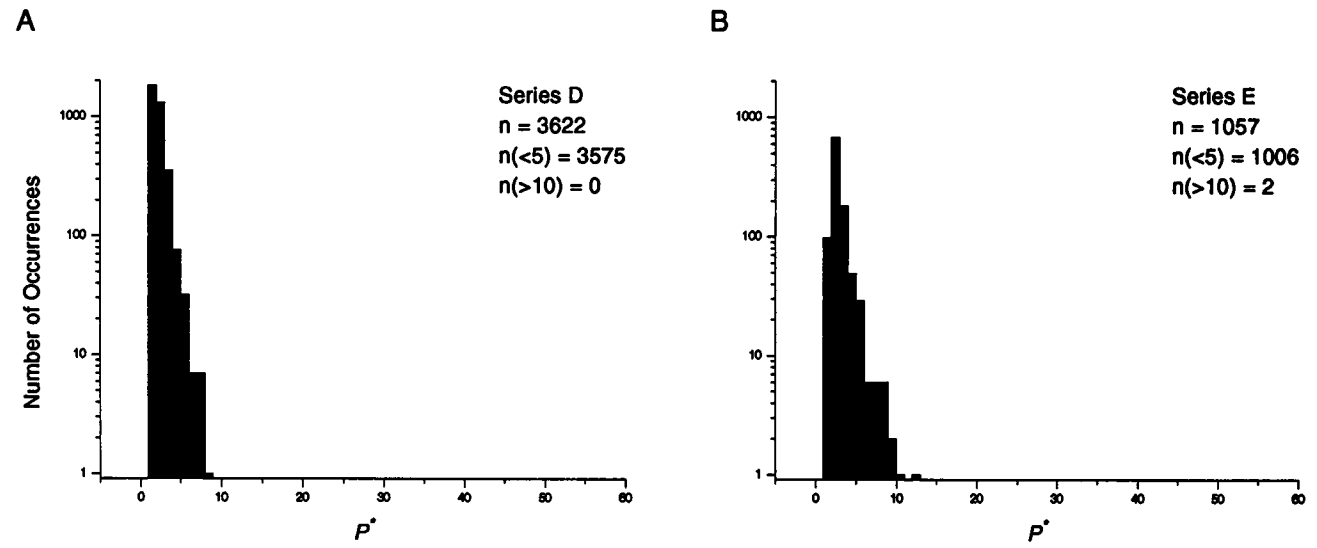

FIGURE 9 Period histograms for series D and E. Period histograms for small oscillations exhibited by series D and E (*A* and *B*, respectively). Printed in the inset of each panel is the number of small oscillations (n), the number of these oscillations with $P^* < 5$, and the number with $P^* > 10$.

activated cation current (I_h), with $\tau_{max} > 100$ ms, and not the relatively fast "delayed" K^+ current, is responsible for repolarizing the neuron during each oscillatory cycle. We ran a series of simulations to test the feasibility of this hypothesis. In these simulations (series E), parameters of the outward current were derived from the dominant component of I_h as we have measured it in cultured neocortical neurons (Budde et al., 1994).

Fig. 4 *E1* shows bifurcation maps generated by series E. The principal difference between these maps and those of Figs. 4 *A1–D1* is that series E-generated maps contain large regions in which v_1 is highly negative. Regions with $v_1 < -2.0$, corresponding to an unreasonable value of the leak reversal potential of < -96 mV and colored black in Fig. 4 *E1*, were not included in subsequent analyses. Other than the illegal regions, the bifurcation maps of series E largely resemble those of series B and C, but with more subthreshold bifurcations. As before, oscillatory period is of the same scale as τ_{max} (Figs. 4 *E2* and 9 *B*). However, unlike the delayed K^+ current, I_h is known to activate on a slow time scale ($\tau_{max} > 100$ ms; Budde et al., 1994). Thus, the dimensional oscillatory period for this model would be ~100 ms, corresponding to the physiologically observed oscillatory frequency range for subthreshold oscillations in mEC layer II neurons.

Oscillations of series E models were relatively insensitive to perturbations in g_{Na}; 30% of small oscillations were

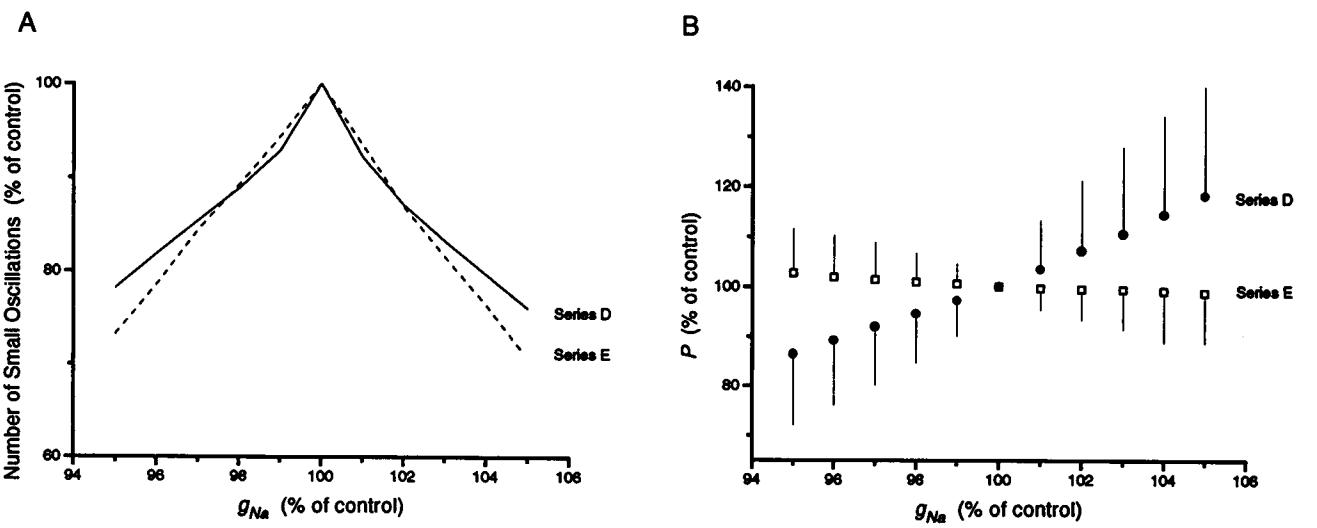

FIGURE 10 Effects of perturbations in g_{Na} on oscillatory behavior in series D and E. (*A*) Number of small oscillations exhibited by series D and E in response to perturbation of g_{Na} from its control value, represented as a percent of control. Control values: 3622 (series D); 1057 (series E). (*B*) Effect of perturbations in g_{Na} on the periods of small oscillations for series D and E. Error bars are standard deviations.

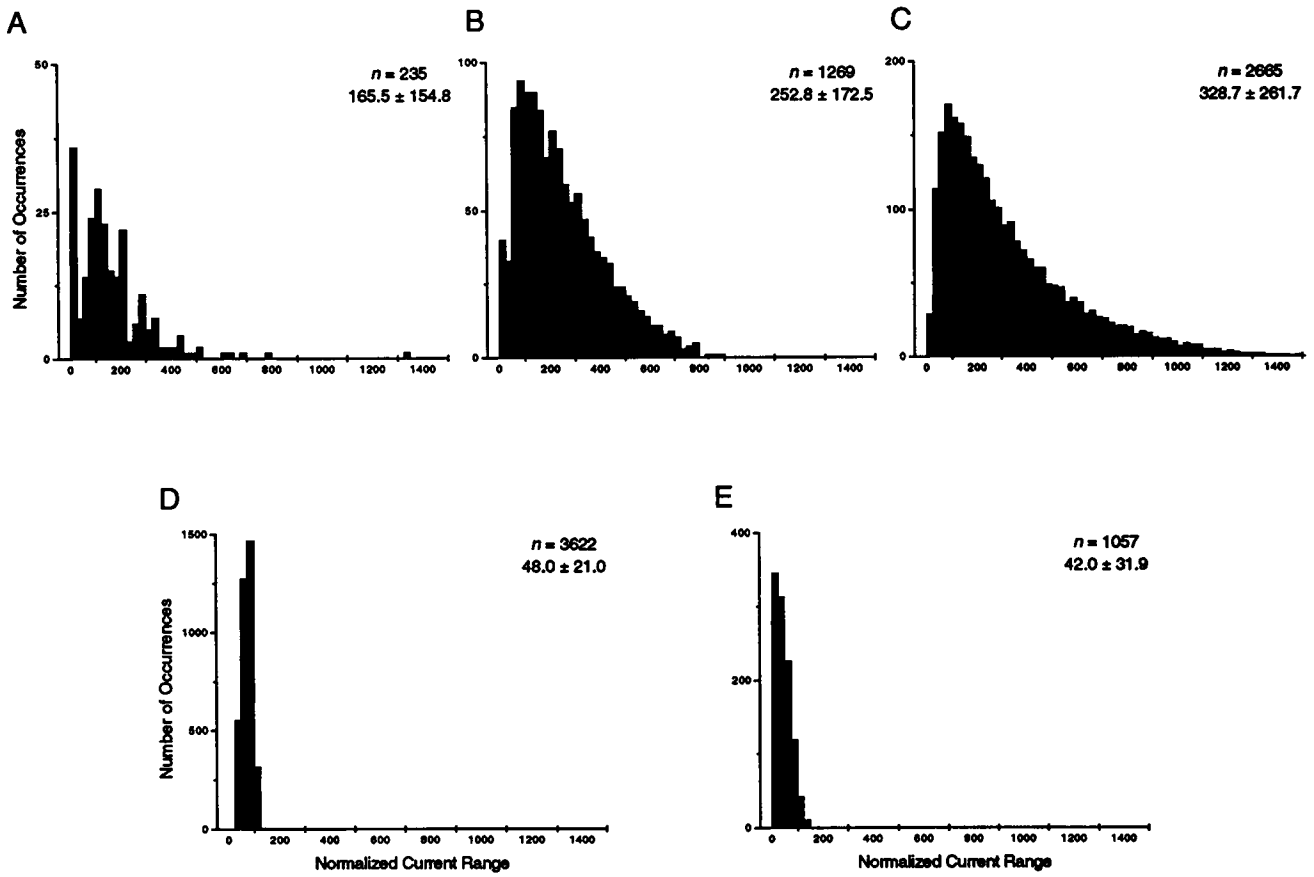

FIGURE 11 Normalized current ranges over which models oscillate. Histograms of normalized current ranges (i.e., $(i_{bif2} - i_{bif1})/i_{bif1} \times 100\%$) over which models in series A–E (panels *A–E*, respectively) oscillate.

obliterated with g_{Na} perturbed by +5% (Fig. 10 *A*; cf. Fig. 7 *A*). Oscillatory period in series E was less sensitive to the value of g_{Na} than that in series A or D, but more sensitive than that in series B and C. Interestingly, the slope of *P* versus g_{Na} is negative only for series E.

In the course of running the series E simulations, we developed the impression that, while these models exhibited oscillatory behavior, this behavior seemed confined to a narrower range of i_{app} than in other series. To test this hypothesis, we measured, for each small oscillation, the current range over which the model would oscillate (i.e., the difference $i_{bif2} - i_{bif1}$). To account for the fact that different models had widely varying input resistances, we normalized the current range, dividing it by i_{bif1}. Histograms of the normalized current range are shown in Fig. 11 for each model series. Models with a low-threshold K^+ current (series B and C) oscillate over a large range of normalized input currents. Models with a steeper Na^+ activation function (series D) or I_h (series E) are sharply limited in the current ranges over which they will oscillate.

DISCUSSION

In this study, we have examined quantitatively the conditions under which a persistent Na^+ current and delayed K^+ current can generate subthreshold oscillations. Gradually rising oscillations were confined to a thin wedge of g_{Na}-g_K space (Fig. 4). The only published description of the delayed K^+ current in mEC cells (Eder et al., 1991) did not match the persistent Na^+ current in threshold; this mismatch compromised the ability of the model to generate subthreshold oscillations. Shifting the threshold of the delayed K^+ current leftward, as in its "modulated" form (Eder et al., 1991), allowed the model to generate subthreshold oscillations. An alternative model in which inward rather than outward rectification underlies the oscillations was shown to be plausible, although this model oscillated over only a small range of applied currents.

Oscillatory period is closely tied to the activation time constant of the outward current (either the delayed K^+ current or I_h). This result, which has been demonstrated for isolated examples in other modeling efforts (Wang, 1993), does not seem surprising, but it seems incompatible with data indicating that the relatively fast delayed K^+ current underlies subthreshold oscillations (Klink and Alonso, 1993). At least four causes could underlie this discrepancy. First, the unusually large period could be generated by spatial separation of Na^+ and K^+ currents. Second, our mathematical description of the persistent Na^+ current could be in error. Third, the delayed K^+ current could

contain a significant slow component in the subthreshold range. Fourth, I_h rather than the delayed K^+ current could underlie subthreshold oscillations.

The explanation that long-period oscillations are generated by spatially segregated currents seems unlikely. Peak responses in a passive cable travel at an approximate velocity of 2 length constants per time constant (Jack et al., 1975). Thus, even with a passive membrane time constant of 100 ms, Na^+ and K^+ currents would need to be ~2 space constants apart in order for propagation time to contribute significantly to a 10-Hz oscillation. At such remote locations, the currents would be effectively isolated from one another.

Our principal simplification, and thus the most likely source of inaccuracy in modeling the Na^+ current was to assume instantaneous kinetics. We have examined models with noninstantaneous Na^+ kinetics in specific instances and have found the contribution of this factor, while not necessarily negligible, does not account for 8-Hz oscillations unless the Na^+ current activation time constant (τ_m) is greater than 1 ms. Fig. 12 shows results from this analysis. For these simulations, we chose τ_{max} = 7 ms (to match our voltage-clamp data for the delayed K^+ current). We set τ_m at one of several constant values, varying from near-instantaneous to 1 ms. Oscillatory frequency near the bifurcation point was plotted versus τ_m. For $\tau_m < 0.1$ ms, oscillatory frequency was above 50 Hz, matching the instantaneous-activation case. For 0.1 ms $< \tau_m <$ 1 ms, oscillatory frequency was affected, but remained above 20 Hz, more than double that seen in physiological recordings. These results imply that only a slowly activating Na^+ current ($\tau_m > 1$ ms) is likely to combine with the delayed K^+ current to generate θ-like oscillations. Although we have not examined systematically the activation kinetics of the persistent Na^+ current, unpublished data from previous studies (White et al., 1993) indicate that such a slow persistent Na^+ current is unlikely.

It seems possible that the delayed K^+ current is dominated by a slow component near rest. This hypothesis seems incompatible with current-clamp data indicating that the Ba^{2+} and TEA-sensitive K^+ current activates rapidly (Klink and Alonso, 1993). However, both Ba^{2+} and TEA are notoriously nonspecific and thus likely blocked multiple currents. These nonspecific effects could lead to large decreases in the leak conductance of the cell, thus increasing the passive membrane time constant and giving the appearance (in current clamp) of having blocked a rapidly activating conductance. Indeed, because the presence of subthreshold oscillations is leak-sensitive (compare adjacent graphs in Fig. 4), the possibility exists that these blockers obliterate oscillations simply by changing the leak conductance of the neuron.

Another conceivable hypothesis is that I_h, and not the delayed K^+ current, is the membrane current responsible for repolarization during subthreshold oscillations. Our simulations (series E) indicate that I_h kinetics seem better matched to observed oscillatory frequencies than do delayed rectifier kinetics. However, the ability of subthreshold oscillations to persist in the presence of Cs^+ (Klink and Alonso, 1993), a potent blocker of I_h, argues strongly against this explanation.

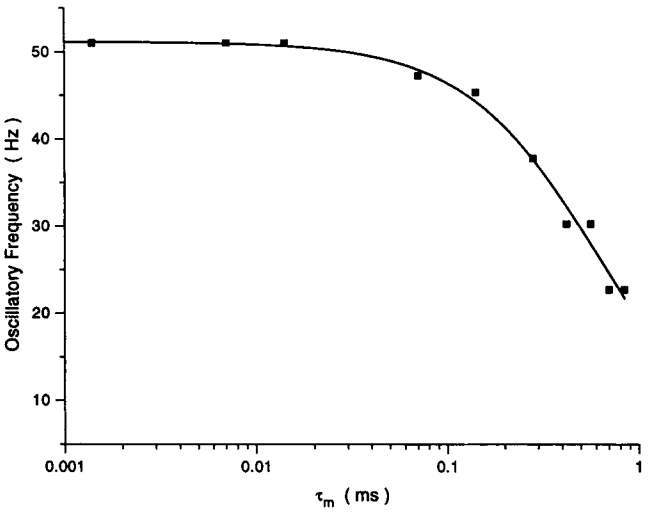

FIGURE 12 Effect of Na^+ current activation time constant on oscillatory period. ■ Dimensional oscillatory period (calculated assuming τ_{max} = 7 ms) vs. τ_m, the activation time constant of the Na^+ conductance. The model was a three-dimensional extension of the series C model, in which the gating variable m was determined from the differential equation $dm/dt = (m_\infty - m)/\tau_m$, where τ_m was held constant at the value given on the x axis. (g_{Na}, g_K, g_L) = (0.8, 4.4, 1.5). In some cases, g_{Na} was altered slightly (by <5%) to preserve existence of the limit-cycle solution. $i_{app} \approx 0.06$. Values of oscillatory period were determined by taking the fast Fourier transform of the time-domain oscillatory trace and determining the fundamental frequency from the magnitude spectrum. The straight line is a least-squares fit of the function $f_{max}/1 + (\tau_m/\tau_{1/2}))$ to the data points.

Two results presented here point toward potential methods of resolving the issue of which hyperpolarizing current–the delayed K^+ current or I_h–underlies subthreshold oscillations. First, the two competing models predict opposite effects of g_{Na} on oscillatory period. For the K^+ current model, dP/dg_{Na} is small and positive (Fig. 7 *B*); for the I_h model, it is negative (Fig. 10 *B*). This result could be put to use by partially blocking the Na^+ current and noting the effect on *P*. Second, K^+ current models oscillate over larger ranges of injected current than do I_h models. Thus, a careful look at this current range in a brain slice preparation might be fruitful, although such experiments might be compromised by interference from other membrane currents at more depolarized levels.

It should be mentioned in closing that both the delayed K^+ current and I_h may make important contributions to subthreshold oscillations in EC stellate cells. Such a mechanism might explain why there has been some confusion regarding the outward current underlying the oscillations (Alonso and Llinás, 1989; Klink and Alonso, 1993), and could conceivably combine desirable attributes of both K^+ current models (oscillations over large current ranges) with those of I_h models (appropriate frequencies).

APPENDIX

In dimensional terms, Eq. 1 can be written:

$$C\frac{dV}{dt} = -G_{Na}m_\infty(V)(V - V_{Na}) - G_K w(V - V_K) - G_L(V - V_L) + I_{app}$$

where C is membrane capacitance (F); V is membrane potential (V); G_{Na}, G_K, and G_L are maximal Na^+, K^+, and leakage conductances (S); V_{Na}, V_K, and V_L are Na^+, K^+, and leakage reversal potentials (V); and I_{app} is applied current (A). Defining $v = V/V_{Na}$ gives:

$$\frac{dv}{dt} = \frac{1}{V_{Na}}\frac{dV}{dt} = \frac{1}{C}[-G_{Na}m_\infty(v)(v - 1) - G_K w(v - v_K) - G_L(v - v_L) + I_{app}/V_{Na}]$$

where lower-case voltages $v_i = V_i/V_{Na}$ for each ionic species. (Note that activation functions and time constants have been implicitly redefined as functions of v.) Defining $g_i = G_i/G_{ref}$ gives:

$$\frac{dv}{dt} = \frac{g_{ref}}{C}[-g_{Na}m_\infty(v)(v - 1) - g_K w(v - v_K) - g_L(v - v_L) + I_{app}/V_{Na}]$$

Finally, normalizing the time variable ($t = t_{old}\,(G_{ref}/C)$) gives Eq. 1 in its normalized form. To return the system to dimensional form, one should pick values of V_{Na} (usually around +48 mV), C (usually 1 $\mu F/cm^2$ × somatic surface area), and G_{ref}, which can be chosen using the relationship $G_{ref} = C/(\phi\tau_{max})$, where τ_{max} is the maximum value of the dimensional outward current activation time constant (in seconds).

We thank A. Alonso, V. Booth, E. Doedel, G. B. Ermentrout, and T. Rögnvaldsson for helpful discussions and technical assistance, and two anonymous reviewers for their thorough comments. XPP was provided by G. B. Ermentrout. Part of this work was performed at the Marine Biological Laboratories in the Methods in Computational Neuroscience course directed by D. Tank and D. Kleinfeld.

Supported by grants from The Whitaker Foundation (to J. A. W.), the Office of Naval Research (to A. R. K.), and the National Institutes of Health (to A. R. K.).

REFERENCES

Alonso, A., and R. M. Klink. 1993. Differential electroresponsiveness of stellate and pyramidal-like cells of medial entorhinal cortex layer II. *J. Neurophysiol.* 70: 128–143.

Alonso, A., and R. R. Llinás. 1989. Subthreshold Na^+-dependent theta-like rhythmicity in stellate cells of entorhinal cortex layer II. *Nature.* 342: 175–177.

Bland, B. H., and L. V. Colom. 1993. Extrinsic and intrinsic properties underlying oscillation and synchrony in limbic cortex. *Prog. Neurobiol.* 41:157–208.

Budde, T., J. A. White, and A. R. Kay. 1994. The hyperpolarization-activated Na^+-K^+ current (I_h) in neocortical neurons is blocked by external proteolysis and internal TEA. *J. Neurophysiol.* 72: 2737–2742.

Christie, B. R., and W. C. Abraham. 1992. Priming of associative long-term depression in the dentate gyrus by theta frequency synaptic activity. *Neuron.* 9:79–84.

Crick, F., and C. Koch. 1990. Towards a neurobiological theory of consciousness. *Semin. Neurosci.* 2:263–275.

Doedel, E. J. 1981. AUTO: A program for the automatic bifurcation and analysis of autonomous systems. *Cong. Num.* 30:265–284.

Eder, C., E. Ficker, J. Gündel, and U. Heinemann. 1991. Outward currents in rat entorhinal cortex stellate cells studied with conventional and perforated patch recordings. *Eur. J. Neurosci.* 3:1271–1280.

Jack, J. J. B., D. Noble, and R. W. Tsien. 1975. Electric Current Flow in Excitable Cells. Oxford University Press, Oxford, UK.

Klink, R. M., and A. Alonso. 1993. Ionic mechanisms for the subthreshold oscillations and differential electroresponsiveness of medial entorhinal cortex layer II neurons. *J. Neurophysiol.* 70:144–157.

Krinskii, V. I., and Y. M. Kokoz. 1973. Analysis of equations of excitable membranes. I. Reduction of the Hodgkin-Huxley equations to a second order system. *Biofizika.* 18:506–511.

Larson, J., and G. Lynch. 1986. Induction of synaptic potentiation in hippocampus by patterned stimulation involves two events. *Science.* 232:985–988.

Morris, C., and H. Lecar. 1981. Voltage oscillations in the barnacle giant muscle fiber. *Biophys. J.* 35:193–213.

Plant, R. E., and M. Kim. 1976. Mathematical description of a bursting pacemaker neuron by a modification of the Hodgkin-Huxley equations. *Biophys. J.* 16:227–244.

Rinzel, J., and G. B. Ermentrout. 1989. Analysis of neural excitability and oscillations. *In* Methods in Neuronal Modeling. C. Koch, and I. Segev, editors. MIT Press, Cambridge, MA. 135–169.

Singer, W. 1993. Synchronization of cortical activity and its putative role in information processing and learning. *Annu. Rev. Physiol.* 55: 349–374.

Strogatz, S. H. 1994. Nonlinear Dynamics and Chaos. Addison-Wesley, Reading, MA.

Vanderwolf, C. H. 1969. Hippocampal electrical activity and voluntary movement in the rat. *Electroencephalogr. Clin. Neurophysiol.* 26: 407–418.

Wang, X.-J. 1993. Ionic basis for intrinsic 40 Hz neuronal oscillations. *Neuroreport.* 5:221–224.

White, J. A., A. Alonso, and A. R. Kay. 1993. A heart-like Na^+ current in the medial entorhinal cortex. *Neuron.* 11:1037–1047.